

Structural and thermal analysis of a MEMS angular gyroscope

Chris C. Painter and Andrei M. Shkel

Microsystems Laboratory, Department of Mechanical and Aerospace Engineering
University of California, Irvine, CA, USA

ABSTRACT

This paper describes the structural and thermal modeling of a Micro Electro Mechanical System (MEMS) z-axis angular gyroscope. The gyroscope consists of a oscillating proof mass supported by a suspension made up of six concentric interconnected rings rigidly attached to an anchored frame.¹ The device is capable of measuring angular displacement through precession of the proof mass line of oscillation in the presence of rotation induced Coriolis force. Using a strain energy method, a closed form solution for the effective stiffness of the suspension system is developed, which is confirmed using finite element modeling. A comparative study of the suspension with a commonly used serpentine spring suspension demonstrates that the studied device is robust to thermal fluctuations and residual stresses. A parametric analysis is used to identify an appropriate micromachining technology suitable for the fabrication of the angular gyroscope.

Keywords: MEMS Gyroscope, Angular Gyroscope, Isotropic Suspension, Structural Modeling of MEMS, Thermal Modeling of MEMS

1. INTRODUCTION

The necessity for low cost, high performance inertial sensors has been the force driving micromachined gyroscopes into the market today. By virtue of sizes and fabrication costs magnitudes lower than their macro world counterparts, micromachined gyroscopes offer a wide range of applications,² ranging from satellite attitude sensing to rollover detection in automobiles. By combining multiple gyroscopes and accelerometers with on-board integrated electronics on a chip, full position and rate sensing can be obtained. Currently, there is an ongoing effort to manufacture gyroscopes with increasingly improved resolution, bandwidth, and reduction of errors.

Most micromachined gyroscopes sense angular rates using vibrational elements. A structure is driven into resonance and rotation induced Coriolis force causes the transfer of energy from the driven vibrational mode to a sense vibrational mode. The magnitude of energy transferred is proportional to the rate of rotation. Inherent in all micromachined gyroscopes are sensing errors that manifest themselves in the form of angle random walk and bias drift.² In applications where it is necessary to integrate the rate signal to obtain the position, these errors are also integrated, thus magnifying the error. In these cases, it is more attractive to measure the angle directly in order to avoid the effect of error integration.

A micromachined gyroscope working in full angle mode operates by first oscillating a structure along two orthogonal drive axes. Input rotation induced Coriolis force causes the line oscillation to precess. This principle is best illustrated by the Foucault pendulum, whose precessing line of oscillation is used to measure the Earth's rotation.³ Although current devices utilizing vibrational shell designs⁴ are capable of full angle sensing, these designs have limited sense capability due to the restriction that all electrodes must be incorporated around the perimeter of the device.

The studied device¹ utilizes a vibrational “lumped mass-spring system” with electrostatic combs used for drive and sense, Fig. 1(a). The use of sense combs interwoven between the comb fingers of the proof mass increases the sense capacitance, and therefore the sense capabilities, of the device. The device operates by driving a proof mass into forced oscillation along two drive axes. Upon reaching the desired amplitude, the drive force is removed and the energy of the system is maintained using a specially designed control architecture.^{1,5} The rotation induced Coriolis

Further author information: (Send correspondence to C.C.P.)

C.C.P.: E-mail: cpainter@uci.edu

A.M.S.: E-mail: ashkel@uci.edu

Web: <http://mems.eng.uci.edu>

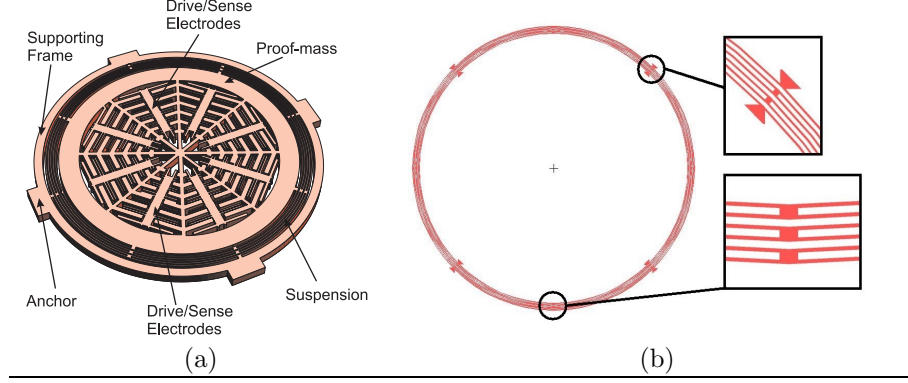


Figure 1. (a) The studied angular gyroscope uses combs to drive a proof mass into oscillation along two drive axes. Rotation induced Coriolis force causes the line of oscillation to precess and the precession angle is proportional to the angular displacement of the device. (b) A proposed suspension design consisting of six interconnected rings rigidly attached to an anchored frame provides necessary isotropy required for the operation of this device.

force causes the line of oscillation to precess and the precession angle is proportional to the angular displacement of the device.

In order for the line of oscillation to precess undisturbed, the gyroscope requires a suspension with equal stiffness along the principle axes of elasticity, or isotropic suspension. Operation of the device with a non-isotropic suspension results in quadrature error manifested as an elliptical oscillation pattern that develops during precession.⁶ This degrades the performance of the gyroscope. In order to satisfy the isotropy condition, a novel concentric ring suspension consisting of six interconnected rings rigidly attached to an anchored frame is utilized, Fig. 1(b).

A structural characterization of the device is performed by utilizing strain energy methods to find a closed form expression for the stiffness of the suspension along the principle axes of elasticity. This analytically obtained result is verified using finite element analysis. A comparative thermal sensitivity study is done between the ring suspension and a serpentine spring suspension, a suspension type commonly used in MEMS applications. Based on the thermal analysis, the effect of residual stress is discussed. Finally, a parametric analysis of the suspension demonstrates the necessity for thick structural layers in order to prevent low frequency undesirable modes of operation.

2. GYROSCOPE PRINCIPLES

For the operation of the gyroscope, a lumped mass-spring system, Fig. 2, is assumed, utilizing three coordinate systems: $\{i, j, k\}$ - inertial, fixed frame system, $\{x, y, z\}$ - coordinate system of the rotating platform, and $\{\tilde{x}, \tilde{y}, \tilde{z}\}$ - precessing coordinate frame attached to the line of oscillation. If the natural frequency of the system is large compared to the input rotation and the stiffness in the z-direction is much larger than the stiffness in the other two orthogonal directions, then the governing equations of motion are given by⁵

$$\begin{aligned} \ddot{x} + \omega_n^2 x - 2\Omega \dot{y} &= 0 \\ \ddot{y} + \omega_n^2 y + 2\Omega \dot{x} &= 0 \end{aligned} \quad (1)$$

If we assume an even mass distribution, then Equation (1) can be decomposed into

$$\begin{bmatrix} m & 0 \\ 0 & m \end{bmatrix} \begin{Bmatrix} \ddot{x} \\ \ddot{y} \end{Bmatrix} + \begin{bmatrix} k_{xx} & k_{xy} \\ k_{yx} & k_{yy} \end{bmatrix} \begin{Bmatrix} x \\ y \end{Bmatrix} + \begin{bmatrix} 0 & -2\Omega \\ 2\Omega & 0 \end{bmatrix} \begin{Bmatrix} \dot{x} \\ \dot{y} \end{Bmatrix} = \begin{Bmatrix} 0 \\ 0 \end{Bmatrix} \quad (2)$$

where m is the mass and k_{xx} , k_{yy} , k_{xy} , and k_{yx} are the effective stiffness terms of the system. Since the stiffness is the same in the x and y directions ($k_{xx} = k_{yy}$ and $k_{xy} = k_{yx} = 0$), any axis in the x-y plane can be considered a principle axis of elasticity. As a result, the line of oscillation precesses undisturbed, Fig. 3(a), in the presence of rotation Ω , allowing accurate measure of the angle of precession ϕ , given by⁵

$$\tan \phi = \frac{2(\omega_n^2 xy + \dot{x}\dot{y})}{\omega_n^2(x^2 - y^2) + (\dot{x}^2 - \dot{y}^2)} \quad (3)$$

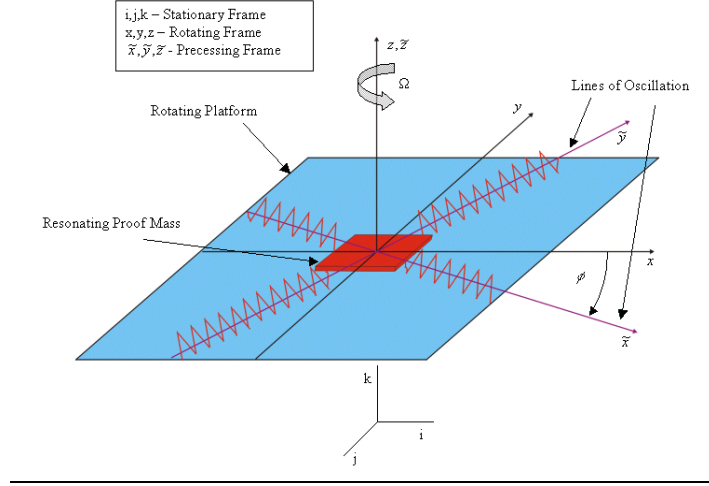


Figure 2. Mass-spring model of the z-axis angular gyroscope. $\{i, j, k\}$ is the inertial, fixed frame coordinates, $\{x, y, z\}$ is the coordinate system of the rotating platform, $\{\tilde{x}, \tilde{y}, \tilde{z}\}$ is the precessing coordinate frame attached to the line of oscillation, and ϕ is the precession angle.

In the case of a non-isotropic suspension where $k_{xx} \neq k_{yy}$ and $k_{xy} = k_{yx} \neq 0$, the location of the principle axes of elasticity is no longer arbitrary. These anisoelasticities disrupt the line of oscillation as it precesses away from the principle axes, Fig. 3(b), resulting in degraded performance of the gyroscope.⁶

3. STRUCTURAL ANALYSIS

This section develops an analytical model to estimate the stiffness and confirm the isotropy of the proposed suspension. The results are verified using finite element modeling.

3.1. Analytical Model of the Suspension

The system consists of a proof mass suspended above the substrate using six concentric rings, Fig. 4(a). The rings are interconnected at 90 degree increments and the outer ring is rigidly attached to an anchored frame. By calculating the deflection of the proof mass in response to a known arbitrary force \vec{F} at an arbitrary angle α , an expression for the stiffness is found. The total deflection of the proof mass is then calculated by summing the contributions of each individual ring through superposition, assuming each ring interconnect is rigid.

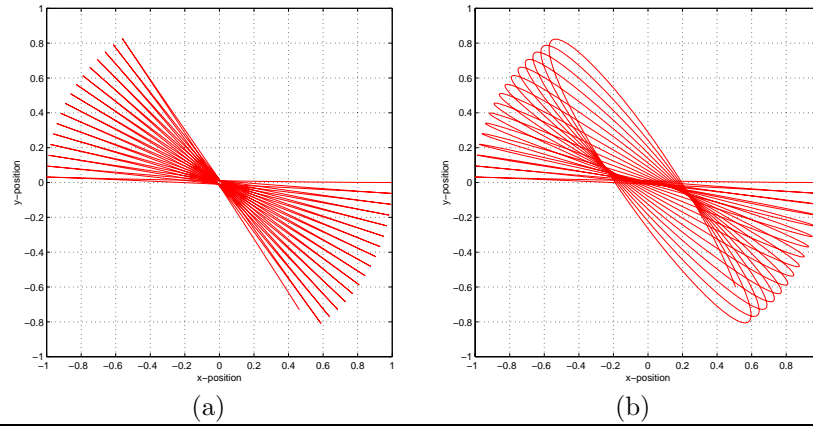


Figure 3. (a) An isotropic suspension allows for the ideal operation of the gyroscope where the line of oscillation precesses undisturbed. (b) A non-isotropic suspension results in quadrature error manifested as an increasing elliptical oscillation pattern during precession.

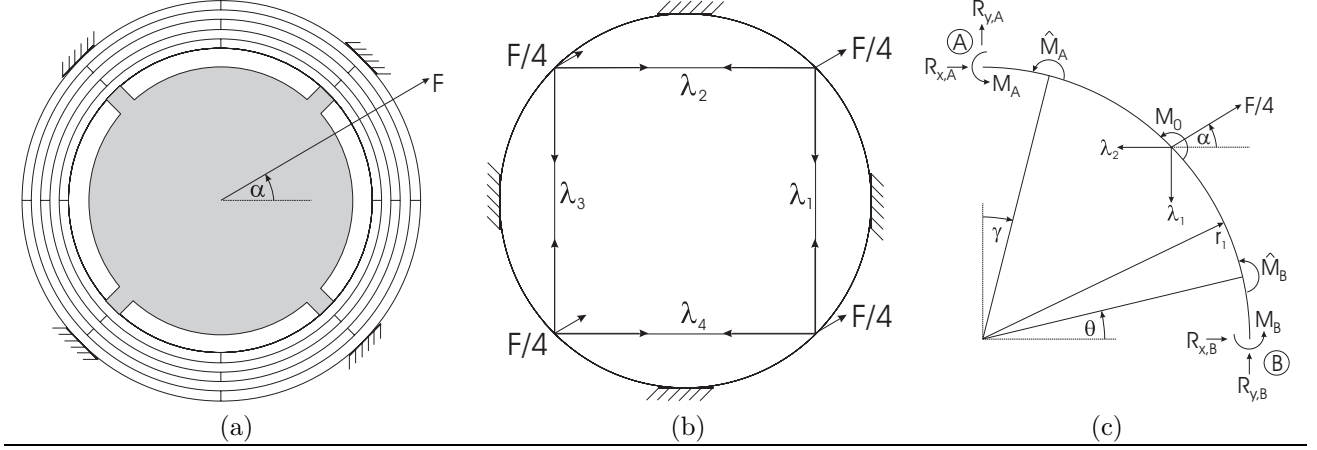


Figure 4. (a) The gyroscope is modeled as a proof mass suspended on a six interconnected ring suspension system. The stiffness of the suspension is calculated by finding the deflection of the proof mass in response to a force \vec{F} at an arbitrary angle α . (b) The total deflection can be decomposed into the contributions of the inner ring and reactions from the subsequent rings. (c) The inner ring contribution can be calculated by the contributions of each quadrant. The λ 's and M_0 represent constraint forces and a constraint moment due to the rigid attachment of the proof mass.

We first find the deflection contribution of the inner ring. The inner ring is fixed at its connection points to the second ring and the rigid connection of the proof mass is modeled using constraint forces ($\lambda_1, \lambda_2, \lambda_3, \lambda_4$), Fig. 4(b). Due to symmetry, this model can be further decomposed to a quadrant of the ring, Fig. 4(c), where the fixed end conditions at ends A and B are modeled using reaction forces and moments (R_x, R_y, M). M_0 represents the moment constraint assuming that the proof mass undergoes no angular deflection.

The corresponding reactions are calculated⁷ as functions of the constraints and applied force and are used to find the total strain energy U of the curved member. If the radius r_1 is large compared to the thickness of the ring t , i.e. $\frac{r_1}{t} > 10$, the bending energy dominates the strain energy,⁷ and U can be expressed as

$$U = \int_0^{\frac{\pi}{4}} \frac{\hat{M}_A^2}{2EI} r_1 d\gamma + \int_0^{\frac{\pi}{4}} \frac{\hat{M}_B^2}{2EI} r_1 d\theta \quad (4)$$

$$\hat{M}_A = -r_1(1 - \cos \gamma)R_{x,A} - r_1 \sin \gamma R_{y,A} + M_A$$

$$\hat{M}_B = r_1 \sin \theta R_{x,B} + r_1(1 - \cos \theta)R_{y,B} + M_B$$

\hat{M}_A and \hat{M}_B are the reaction induced moments at angles γ and θ from fixed ends A and B, respectively (see Fig. 4). By Castilano's theorem, the deflection of an elastic member in the direction of the applied force is equal to the change in strain energy with respect to the applied force,⁷

$$\delta_{F,r_1} = \frac{\partial U}{\partial F} = \frac{r_1}{EI} \int_0^{\frac{\pi}{4}} \hat{M}_A \frac{\partial \hat{M}_A}{\partial F} d\gamma + \frac{r_1}{EI} \int_0^{\frac{\pi}{4}} \hat{M}_B \frac{\partial \hat{M}_B}{\partial F} d\theta \quad (5)$$

A similar solution is arrived at for each of the four quadrants, leading to a total of eight unknowns consisting of the four λ constraints and the four M_0 constraints. By assuming zero deformation in the constraints, the unknowns are eliminated by symmetry constraints

$$\delta_{\lambda_1,UR} + \delta_{\lambda_1,LR} = \delta_{\lambda_2,UR} + \delta_{\lambda_2,UL} = 0$$

$$\delta_{\lambda_3,UL} + \delta_{\lambda_3,LL} = \delta_{\lambda_4,LL} + \delta_{\lambda_4,LR} = 0$$

$$\delta_{M_0,UR} = \delta_{M_0,LR} = \delta_{M_0,LL} = \delta_{M_0,UL} = 0$$

Here UR, LR, LL and UL designate the upper right, lower right, lower left, and upper left quadrants of the inner ring, respectively. Solving the system of equations simultaneously yields

$$\delta_{F,r_1} = \frac{r_1^3}{4EI} (4.017e^{-4} F) \quad (6)$$

We now find the contribution of the second ring by modeling it as rigidly attached where it would be connected to the third ring. The reaction forces of the inner ring are used as the applied forces on the second ring. Using the same solution procedure as for the inner ring, with the simplification that the second ring is unconstrained ($\lambda = M_0 = 0$), the deflection of the top and bottom quadrants of the second ring become

$$\delta_{F,r_2} = \frac{F}{EI} (.0002r_2^3 \cos^2 \alpha - .0001r_2^2 r_1 \cos^2 \alpha + .0001r_2^3 \sin^2 \alpha) \quad (7)$$

We invoke a change of variable such that $r_1 = r_2 - \Delta r$, where Δr is the spacing between the rings. If the spacing is sufficiently small compared to the radius ($\Delta r \approx 0$), then (7) simplifies to

$$\delta_{F,r_2} = \frac{r_2^3}{4EI} (4.0104e^{-4} F) \quad (8)$$

With this simplification, the same result is found for the left and right quadrants. Assuming that the bending moment of inertia (I) and the modulus of elasticity (E) are identical for all rings, we see that this deflection varies only with radius when compared to the deflection of the inner ring (6). By induction, this expression for the ring deflection will propagate to each subsequent ring. The generalized stiffness can be approximated by force divided by deflection

$$k_r(r) = 9957.68 \frac{EI}{r^3} \quad (9)$$

The total stiffness of the system can be approximated by summing the stiffness of all the rings in series

$$\frac{1}{k_{tot}} = \sum_{i=1}^n \frac{1}{k_i} \quad (10)$$

The final solution is not a function of α , so it is concluded that this stiffness is the same regardless of the angle of the applied force, thus verifying the isotropy of the suspension.

3.2. Finite Element Modeling

To verify the analytical calculation, a finite element model was constructed using the ANSYS multiphysics software package. The suspension and proof mass were modeled using three dimensional shell elements with a thickness of two microns (assuming surface micromachining technology). The radius of the rings used for simulation were 303.5, 306.5, 309.5, 312.5, 315.5, and 318.5 μm and the width of each ring was 2 μm . A known force of 4 μN was applied at the center of the proof mass in three varying in-plane directions (0, 45, and 60 degrees). The in-plane radial deflections of the proof mass were found to be the same in all three cases, Fig. 5. Due to the symmetry of the structure, this demonstrates that the suspension is uniformly stiff in all radial directions. The stiffness, calculated as force divided by deflection, results in a value of 5.24 $\frac{\text{N}}{\text{m}}$. The analytical calculation gives a stiffness of 6.21 $\frac{\text{N}}{\text{m}}$, yielding a difference of 15.6%. This discrepancy can be attributed to the use of shell elements in the finite element analysis as well as the $\Delta r \approx 0$ and rigid interconnect assumptions from the analytical calculation.

4. THERMAL ANALYSIS

4.1. Global Heating

The effect of temperature changes on the operational resonant frequencies of the system were found through finite element simulation of the device between the temperatures of -100 and 100 $^\circ\text{C}$ and compared to a similar analysis of a device utilizing a serpentine suspension.⁸ The serpentine suspension, Fig. 6(a), consists of three meanders and an appropriate choice of 38.67 μm for connector length L_C , 68.26 μm for span length L_S , and two microns for beam thickness and beam width was made to match the stiffness of the ring suspension system. Each system was modeled assuming an effective mass of 4.18e-10 kg. Temperature loading was first applied uniformly to each model and the nodal displacements due to deformation were found. A modal analysis was then performed with the deformed systems to determine the resonant frequencies and mode shapes. The Young's modulus, E, and the coefficient of thermal expansion, TC_h , were assumed to be 169 GPa and 2.6e-6 $^\circ\text{C}^{-1}$, respectively. To reflect its inherent temperature dependence, E was modified prior to the modal analysis by $ETC_E \Delta T$ where TC_E is the temperature coefficient of Young's modulus for fine-grained polysilicon given as⁹ -75 ppm/ $^\circ\text{C}$ and ΔT is the change in temperature from initial temperature 0 $^\circ\text{C}$.

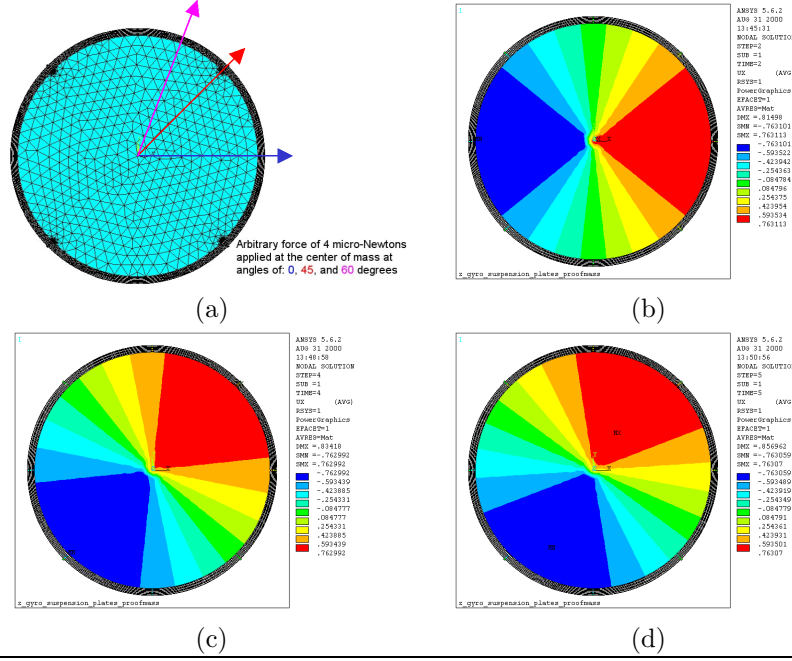


Figure 5. The uniformity of the suspension is confirmed by modeling the system using the FEM package ANSYS. The system is modeled using 3D shell elements. The proof mass is subject to the same load in the directions of (a) 0 ,45, and 60 degrees. The corresponding radial displacements as shown in (b), (c), and (d), respectively, are equal, which confirms the isotropy of the suspension.

In general, the temperature dependence of Young's modulus dominates the change in resonant frequency ω_r , which can be approximated as $\omega_r TC_f \Delta T$, where TC_f is the temperature coefficient for the resonant frequency and can be expressed by¹⁰

$$TC_f = \frac{1}{2}(TC_E - TC_h) \quad (11)$$

However, deformations due to thermal expansion, Fig. 6(b), can, in addition, lead to non-uniform changes in stiffness, resulting in mismatches in the operational mode resonant frequencies. Due to symmetry of the structural displacements, the operational modes frequencies of the ring suspension show a frequency mismatch of only .005%

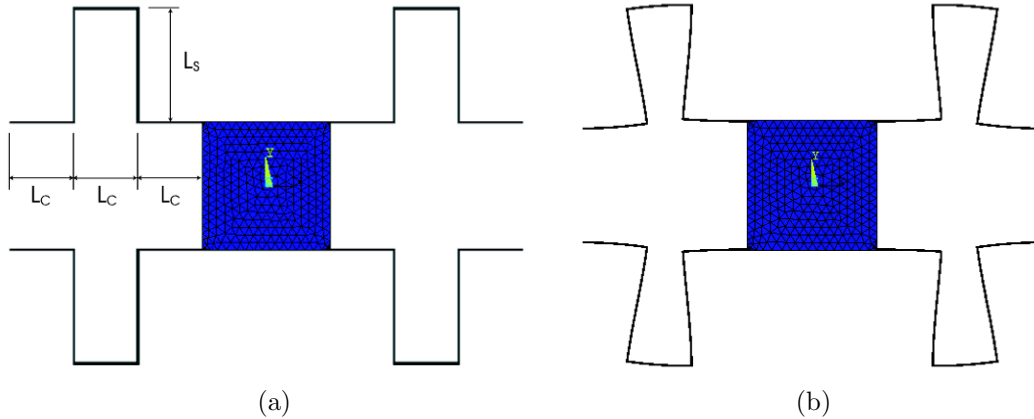


Figure 6. (a) A comparison thermal analysis is done with a device utilizing a serpentine spring suspension. The operational mode resonance frequencies are identical to the ring suspension system through appropriate choices for L_C and L_S . (b) Deformations due to thermal expansion lead to non-uniform changes in stiffness, resulting in mismatches in the operational mode resonant frequencies. The displacements have been exaggerated for clarity.

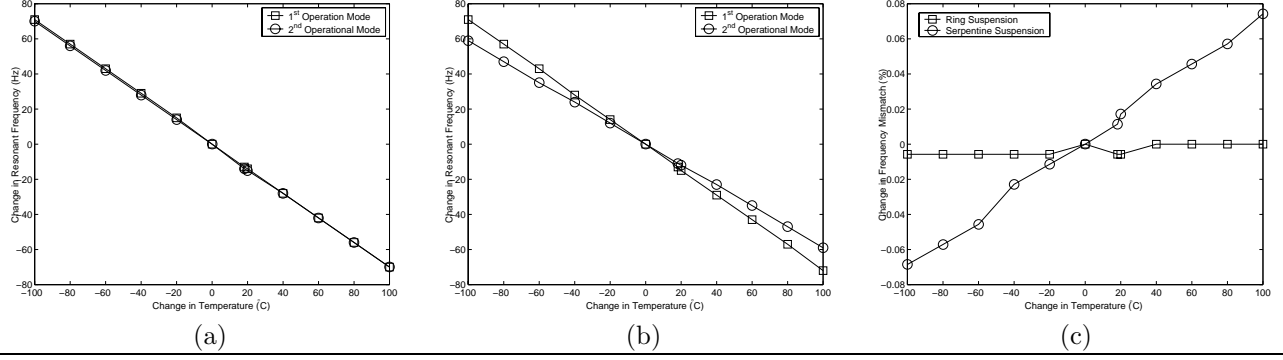


Figure 7. The temperature dependence of Young’s modulus dominates the change in system resonant frequencies as the two operational modes shift by (a) .4% for both modes in the ring suspension and (b) .4% and .33% for the first and second modes respectively in the serpentine suspension. (c) The ring suspension preserves the mode matching during temperature changes, with a .005% change in frequency mismatch at the extreme temperatures. The change in frequency mismatch of the serpentine suspension is an order of magnitude higher at .074%

with a uniform change of .4% from the original values of 17366 and 17367 Hz at the extreme temperatures of -100 and 100 °C, Fig. 7(a). In the case of the serpentine suspension, thermal expansion effects result in an overall change of .4% and .35% in the first and second operational resonant frequencies from original values of 17494 and 17522 Hz respectively, Fig. 7(b), resulting in a frequency mismatch of .074%, an order of magnitude higher than the ring suspension, Fig. 7(c). Although this frequency mismatch is small, even deviations as low as 1% between drive and sense mode frequencies in rate gyroscopes result in errors as high as 20% in the output signal gain.¹¹ A micromachined gyroscope utilizing a more complex non-isotropic suspension is even more susceptible to thermal expansion effects, which is detrimental in cases where high precision is needed.

4.2. Residual Stress

Residual stress is a common byproduct in any MEMS fabrication process involving induced stresses in the photoresist and silicon oxide. As an example, we consider the case of the studied gyroscope being fabricated using the Cronos MUMPS process where heated polysilicon is deposited on a sacrificial oxide layer. Since the polysilicon is rigidly attached to the sacrificial layer, thermal stress develops as the polysilicon cools to room temperature due to thermal mismatch between the polysilicon and the oxide. After subsequent release of the oxide layer, a certain amount of residual stress remains, which varies from run to run. The gyroscope utilizes the POLY1 structural layer, where the residual stress for the MUMPS-39 run, for example, is given as 8 MPa. Since stress can be calculated by $\sigma = E\alpha\Delta T$, the residual stress is analogous to thermally loading the device to a temperature of 18.2 °C. From the previous section, we see that operational modes of the ring suspension remain matched under such temperature loading. In contrast, if a serpentine type suspension were to be implemented using the same technology, the residual stress would result in a frequency mismatch of .011%.

5. MODE MATCHING

For the operation of the gyroscope, it is desirable to design the device where the operational modes are separated from the undesirable modes. Surface micromachining has limitations on the thickness of structural layers and these restrictions yield a low out-of-plane stiffness, resulting in undesirable low frequency out-of-plane modes, Fig. 8(a). A modal analysis using the same shell model from Sect. 3.1 demonstrates that the out-of-plane resonant frequency (2803 Hz) is much lower than the two in-plane operational mode resonant frequencies (17366 and 17367 Hz). It is possible to compensate for this effect by utilizing thicker structural layers.

As the thickness of the structural layer is increased, the in-plane bending moment of inertia, and therefore the in-plane stiffness of the rings, increases linearly ($k_r = f(t)$), Fig. 8(b). In comparison, the out-of-plane moment of inertia, and thus the out-of-plane stiffness, increases as thickness cubed ($k_z = f(t^3)$). If the mass also increases linearly with thickness, the in-plane natural frequencies will remain constant ($\omega_{n,r} = \sqrt{\frac{k_r}{m}} = \text{const}$), while the out-of-plane natural frequencies will increase linearly ($\omega_{n,z} = \sqrt{\frac{k_z}{m}} = f(t)$), Fig. 8(c).

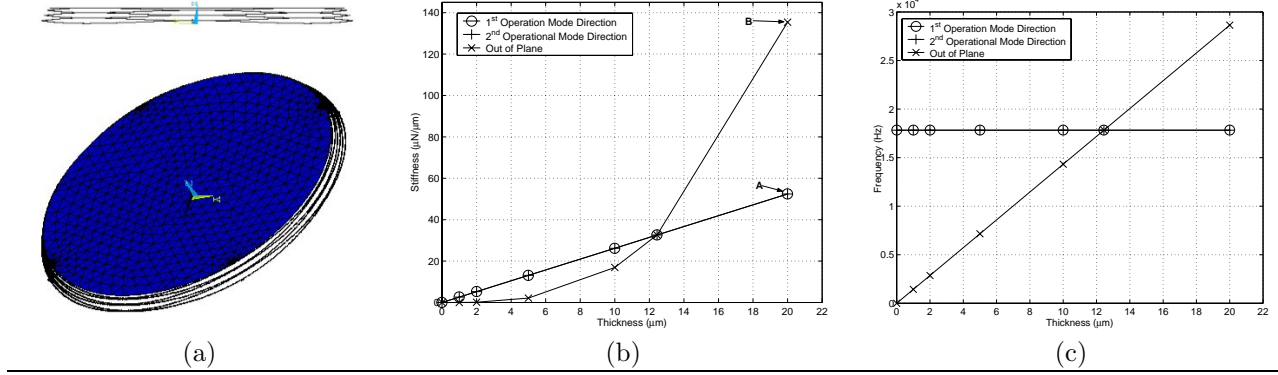


Figure 8. (a) The use of thin structural layers in the design of the suspension results in low frequency out-of-plane modes. (b) The parametric analysis of the suspension reveals that the out-of-plane stiffness increases as thickness cubed, while the in-plane stiffness is linear. At 20 microns thickness, the out-of-plane stiffness (Point **B**) is nearly three times larger than the in-plane stiffness (Point **A**). (c) Since mass also increases linearly, the in-plane natural frequency remains constant while the out-of-plane natural frequency increases linearly.

From a parametric analysis of the suspension, at an optimal thickness of 20 microns, the out-of-plane stiffness is almost three times greater than the in-plane stiffness, thus providing an appropriate mode separation between desirable and undesirable modes of operation of the gyroscope.

6. CONCLUSION

In this paper, we have characterized a MEMS angular gyroscope by evaluating the stiffness of the spring suspension system and determining the resonant modes of operation and corresponding resonant frequencies. It has been demonstrated that the novel six concentric and interconnected ring suspension provides the necessary isotropy required for the operation of the device. Further, we have developed a close form solution for the stiffness of the suspension, which is applicable towards any suspension of this type, given any arbitrary number of rings. The analytical model is confirmed using a finite element analysis method. A thermal comparison between the existing device and a device utilizing a serpentine spring suspension shows that the ring suspension is more resilient to temperature changes as well as residual stress effects that develop during fabrication of the device. It has also been shown that using a fabrication technology utilizing thick structural layers shifts the undesirable modes of operation to a higher frequency range, thus increasing the immunity of the device to undesirable excitations.

REFERENCES

1. A. Shkel and R. T. Howe, "Polysilicon Surface Micromachined Rate Integrating Gyroscopes." UC-Berkeley Office of Technology and Licensing. Case Number B99-077.
2. N. Yazdi, F. Ayazi, and K. Najafi, "Micromachined Inertial Sensors," *Invited Paper, Proceedings of the IEEE*, pp. 1640–1659, August 1998.
3. J. B. L. Foucault, "Démonstration Physique au Mouvement de Rotation de la Terre au Moyen du Pendule," in *C. R. Acad. Sci.*, vol. 32, pp. 135–138, August 1851. (In French).
4. M. Putty, and K. Najafi, "A Micromachined Vibrating Ring Gyroscope," in *IEEE Solid State Sensors and Actuators Workshop*, pp. 213–220, (Hilton Head Island, SC), June 1996.
5. A. Shkel, R. Horowitz, A. Seshia, and R.T. Howe, "Dynamics and Control of Micromachined Gyroscopes," in *The American Control Conference*, (San Diego, CA), June 1999.
6. A. Shkel, R.T. Howe, and R. Horowitz, "Modeling and Simulation of Micromachined Gyroscopes in the Presence of Imperfections," *International Workshop on Micro Robots, Micro Machines and Systems*, September/October 1999.
7. W. C. Young, *Roark's Formulas for Stress and Strain*, McGraw-Hill, Inc., 6th ed., 1989.
8. G. K. Fedder, *Simulation of Microelectromechanical Systems*. PhD thesis, UC Berkeley, 1994.

9. L. Lin, R.T. Howe, and A.P. Pisano, "Microelectromechanical Filters for Signal Processing," *Journal of Microelectromechanical systems* **7**, pp. 286–294, September 1998.
10. T. Rentema and L. Lin, "Active Frequency Tuning for Microresonators by Localized Thermal Stressing Effects," *Solid-State Sensor and Actuator Workshop*, pp. 363–366, (Hilton Head Island, SC), June 2000.
11. E. Netzer and I. Porat, "A Novel Vibratory Device for Angular Rate Measurement," *J. of Dynamic Systems, Measurement and Control*, December 1995.